

Hierarchical materials from fused silk

Received: 21 August 2025

Accepted: 25 March 2026

Published online: 12 May 2026

 Check for updates

Qichen Zhou^{1,2}, Xiangyan Yu³, Chongyang Zeng¹, Sarah Stadlmayr⁴, Sang Hyun Lee^{5,6,7}, Wenqi Wang², Yushu Wang⁸, Bumchul Park^{6,7,9,10}, John Kim^{6,7,9}, Brooke Longo⁸, Glenn Leung⁸, Jens Najorka¹¹, Xiaofeng Wang^{12,13}, Silvestre Pinho¹, Christine Radtke⁴, Wei Tan¹², Han Zhang^{2,14}, Dimitrios G. Papageorgiou¹², David L. Kaplan⁸, Nicholas A. Kotov^{1,6,7,9}✉, Chunmei Li⁸✉ & Emiliano Bilotti¹✉

Silk is an extraordinary natural material whose unique chemistry and hierarchical organization enable performance beyond that of many synthetic counterparts. However, its poor processability arising from the molecular folding patterns of fibroin makes fabricating shapes other than fibres conceptually challenging. Here we report a simple and rapid thermomechanical process to fuse silk fibres into solid materials of arbitrary shapes. This approach avoids silk dissolution and subsequent regeneration – processes typically associated with a substantial environmental footprint due to extensive solvent use. The resulting fused silk exhibits remarkable mechanical properties (flexural strength up to 510 MPa, tensile toughness up to 45 MJ m⁻³), optical transparency in the visible range, pronounced optical activity in the terahertz range with large polarization rotation and processing-dependent biocompatibility and biodegradability. The molecular organization of fused silk emerges from interdiffusion of the naturally present amorphous phase, generating strong intrafibre and interfibre molecular bonds without damaging the original hierarchical organization and the crystalline regions. This direct conversion of natural silk fibres into structural and optically active materials enhances the prospects for scalable production and real-world deployment.

Silk, primarily synthesized by arthropods such as silkworms and spiders^{1,2}, is a marvel of nature. They exhibit outstanding mechanical properties^{2–4}, biocompatibility⁵ and (bio)degradability⁶. The origin of the unique combination of the physical properties of silk is hypothesized to be a result of its complex hierarchical organization, combining ordered and disordered nanoscale sections, which has undergone natural evolutionary refinement over hundreds of millions of years^{7–11}.

In addition to traditional textiles, there has been a resurgence of interest in silk as a high-tech material over the past few decades that led to its implementation in biomedical engineering¹², energy generation¹³, food preservation¹⁴, sensors¹⁵ and other areas. Natural silk fibroin produced by *Bombyx mori* has a complex network of non-covalent hydrogen bonds resulting in multiscale organization of protein segments^{16,17}. This secondary hierarchical structure confers outstanding mechanical

properties but also results in a high glass-transition temperature (T_g , 200–220 °C) and a melting point higher than the degradation temperature^{18,19}, which makes silk fibroins difficult to process. Therefore, most research activities related to silk rely on solution processing methods, involving the dissolution of silk fibres into a solvent (typically, an aqueous solution of lithium bromide, hexafluoroisopropanol (HFIP) or ionic liquids (ILs)), followed by further processing to form different regenerated silk materials^{20–22}. These canonical methods have broadened the scope of silk applications but at the expense of a high economic and environmental footprint partially negating its advantage as an Earth-friendly material. The process of converting silk into advanced materials typically involves large amounts of water, chemicals and time (days to weeks)²³. Most importantly, these methods disrupt the inherent multiscale organization of silk, compromising

A full list of affiliations appears at the end of the paper. ✉ e-mail: kotov@umich.edu; chunmei.li@tufts.edu; e.bilotti@imperial.ac.uk

its original physical properties^{24,25}. Recent studies have revealed that regenerated silk powder can exhibit processability characteristics similar to thermoplastic polymers²⁶, but only after suppressing the crystalline phase and shifting the structural organization towards largely disordered agglomerates.

Here challenged and inspired by these findings, we report a simple and time/cost-efficient thermomechanical method to convert silk fibroin fibres directly into solid materials with record-high mechanical properties, surpassing the specific strength/stiffness and toughness of previously presented silk-based bulk materials, but also tough natural materials such as wood and even glass fibre reinforced polymer (GFRP) composites²⁷. Biodegradability and biocompatibility are tuneable by changing processing conditions. At elevated temperatures and under external pressure, the amorphous phase inherent in any silk fibre—from silkworm silk to spider silk—undergoes forced-flow diffusion, forming dense solid materials without affecting the original hierarchical microstructure. Furthermore, the produced fused silk is optically transparent in the visible range while revealing exceptionally strong polarization rotation in the terahertz (THz) range of electromagnetic frequencies. This processing method paves the way for the simple fabrication of sustainable and high-performance silk materials of arbitrary shape factor, expanding the application scenarios and providing added value to silk and other proteinaceous natural fibres, including end-of-life recycled textiles, as well as broadly emerging applications in THz optics and biomedicine.

Fabrication and morphology

To fabricate the fused silk, commercial reeled *B. mori* silk (Fig. 1a) was first degummed to remove the sericin—the adhesive coating on silk fibroins (Supplementary Fig. 1). This step retains the mechanical properties of the fibroin fibres (Supplementary Figs. 2 and 3) and enables their unidirectional (UD) alignment (Fig. 1b). Such a UD preform (Fig. 1c and Supplementary Fig. 4) was then subjected to hot-pressing (Fig. 1d) under different combinations of processing temperatures and pressures (Fig. 1e). Three main zones can be identified in the phase diagram: non-fused zone, fused zone and chemical degraded zone (Extended Data Fig. 1). Low pressures and temperatures could not densify the silk fibres nor modify the initial optically opaque, porous and fibrillar structure (non-fused zone). Too high pressure and temperature led to dark, translucent and brittle materials (degraded zone). However, a broad processing window exists, where densified, tough and optically transparent bulk materials could be obtained (Fig. 1f). The phase diagram reveals that the processing temperature is the predominant factor. A minimum level of pressure is also essential, depending on the temperature used (for example, ~ 0.06 GPa at ~ 215 °C). Scanning electron microscopy (SEM) images of the transverse and longitudinal cross-sectional areas show the fibre orientation, porosity and interfibre fusion of materials at representative processing conditions in the phase diagram. At 95 °C and 0.5 GPa (at the lower boundary of the phase diagram; Fig. 1g), the material exhibits a mixed morphology, where some silk fibres are fused while interfibre gaps and porosities are still present. When the processing temperature was increased (Fig. 1h,i; 155 °C, 1.0 GPa; 185 °C, 0.2 GPa), silk fibres became more intimately fused into each other. At these conditions, the fibre texture and the interfibre boundaries can still be distinguished in the SEM images. At a higher processing temperature (Fig. 1j; 215 °C, 1.0 GPa), close to the T_g of silk (Supplementary Fig. 5), the morphology of the material appears more homogenous and smoother. Approaching the temperature of silk degradation (Fig. 1k; 245 °C, 0.5 GPa), the cross-section of the material exhibits a brittle fracture morphology, with longitudinal lamellar features aligned along the main fibre direction. Concerning the specific contribution of the processing pressures, it is evident that, at any processing temperature, higher pressure resulted in a slight increase in the density of the fused silk (Supplementary Fig. 6).

Retention of the complex hierarchical organization

A multiscale characterization (Fig. 2) enabled us to understand the structure and underlying mechanism in the produced fused silk.

The fused silk processed at low temperatures (for example, 65 °C) displays a similar endothermic peak as found with unprocessed degummed silk fibres, which is characteristic of water evaporation (Fig. 2a). For increased processing temperatures (215 °C and 245 °C), the endothermic peak corresponding to water evaporation progressively decreases until almost disappearing; this is consistent with the reduction in the specific surface area available to water absorption, caused by the fusion of silk fibres (Fig. 1g–k).

At the nanoscale, the two-dimensional (2D) small-angle X-ray scattering (SAXS) pattern of degummed silk (Fig. 2b) exhibits pronounced equatorial diffuse scattering due to the presence of oriented nanovoids between the nanofibrils²⁸. However, the samples fabricated at 215 °C and 1.0 GPa do not display these characteristics. Recent studies on the hierarchical structure of silk have revealed that it consists of numerous nanofibrils, ~ 3 nm in diameter, with rough surfaces that comprise alternating largely disordered amorphous phase and highly-ordered crystalline regions^{17,29}. This suggests that during hot-pressing, the amorphous phase within the nanofibrils undergoes forced-flow transition, filling the original nanovoids and causing the interfaces of the nanofibrils to merge, resulting in the fusion of the silk fibroin.

The 2D wide-angle X-ray scattering (WAXS) patterns show almost no change in the crystal microstructure with different processing conditions (Fig. 2c and Supplementary Fig. 9). Importantly, the crystallinity of ordered regions remains essentially unchanged within the processing temperature range of 125 °C to 215 °C (Fig. 2d). The crystallite orientation (Fig. 2e), along the fibre direction, only slightly decreases as a result of the relaxation of the amorphous phase at increased temperatures. Similarly, at the scale of protein secondary structure, no notable change in either β -sheet or random coil/ α -helix content was observed after hot-pressing within this temperature range (Fig. 2f and Supplementary Fig. 10). These results indicate that the thermomechanical method preserves the original structure and composition of silk when processed between 125 °C and 215 °C. At 245 °C, however, we observe an apparently contradictory combination of increased relative crystallinity and decreased β -sheet content. This arises because silk undergoes severe thermal degradation at this temperature. The amorphous phase, which has lower thermal stability, degrades before the crystalline phase, thereby increasing the apparent crystallinity^{30–33}. At the same time, the high temperature also causes the protein secondary structures to degrade (the degradation products, such as aromatic compounds, increase the intensity in Fourier transform infrared (FTIR) spectra at around $1,650$ cm^{-1}), leading to an artificially high relative content of random coil/ α -helix and hence a lower apparent β -sheet content^{31,34,35}. The emergence of a new phase transition in the differential scanning calorimetry (DSC) trace (Fig. 2a) and the dark-brown colour of the samples fabricated at 245 °C further corroborate the severe chemical degradation of silk and the generation of carbon condensation products.

At relatively low temperatures ($T < T_g = 213$ °C), water enhances the molecular mobility of the amorphous phase. By contrast, at high temperatures ($T \approx T_g$), the thermally activated mobility of amino acid sequences is predominant. Hence, water molecules serve as plasticizers in low-temperature self-diffusion, increasing mobility of the amorphous phase (Extended Data Fig. 2). In addition, maintaining pressure during the cooling process is also necessary for forming densified and transparent fused silk, which prevents the fused interface from separating as a result of contraction-induced cooling (Supplementary Fig. 11).

Overall, it can be concluded that diffusion of the amorphous segments within the nanofibrils is the key mechanism for the formation of fused silk, enabled by water plasticization and thermally activated molecular mobility within the amorphous phase (Fig. 2g). Processing

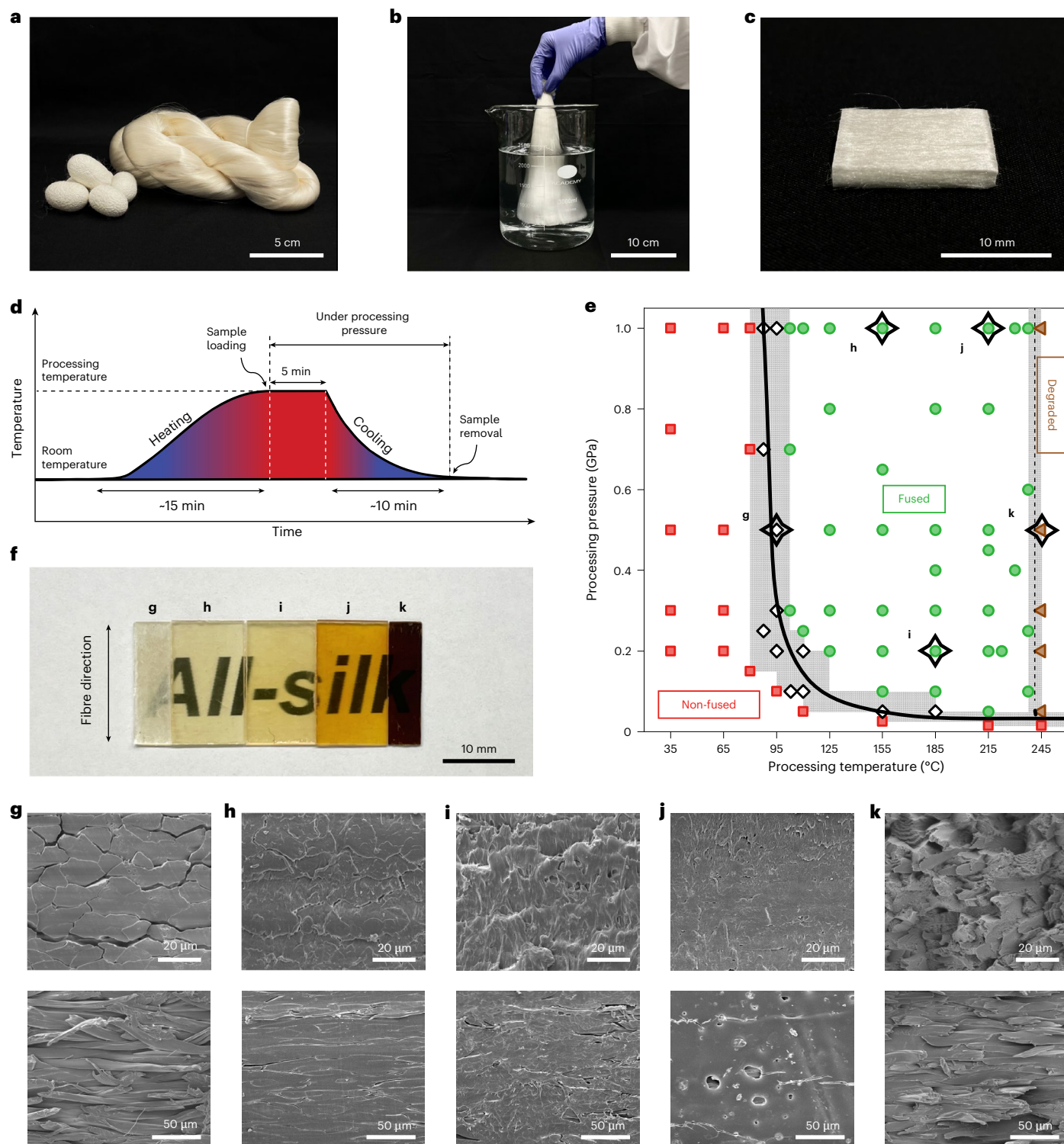


Fig. 1 | Fabrication and morphology. **a**, Commercial reeled *B. mori* silk bundle (right) next to *B. mori* silkworm cocoons (left). **b**, Lifting a silk bundle out of a water bath enhances uniaxial orientation and densification. **c**, Photograph of dry uniaxially aligned degummed silk before hot-pressing. **d**, Typical temperature and pressure profile of the thermomechanical method. **e**, Phase diagram of processing conditions at different temperatures and pressures. Non-fused samples are shown as squares, fused samples as circles, degraded samples

as triangles and transition states as diamonds. Shaded regions indicate the transition boundaries between the three main zones. **f**, Photographs of fused silk fabricated at representative processing conditions in **e**. **g–k**, SEM images of fused silk fabricated at 95 °C, 0.5 GPa (**g**); 155 °C, 1.0 GPa (**h**); 185 °C, 0.2 GPa (**i**); 215 °C, 1.0 GPa (**j**); and 245 °C, 0.5 GPa (**k**), corresponding to the representative processing conditions shown in **e**.

temperatures lower than the thermal degradation temperature of silk (~250 °C) prevent the degradation of the amorphous phase and β -sheet (and other protein secondary structures), preserving the original hierarchical silk structure.

Remarkable mechanical properties

Figure 3a shows the flexural stress–strain curves for fused silk fabricated at different processing temperatures and 0.2 GPa pressure. A record-high flexural strength of 510 ± 50 MPa, flexural modulus of

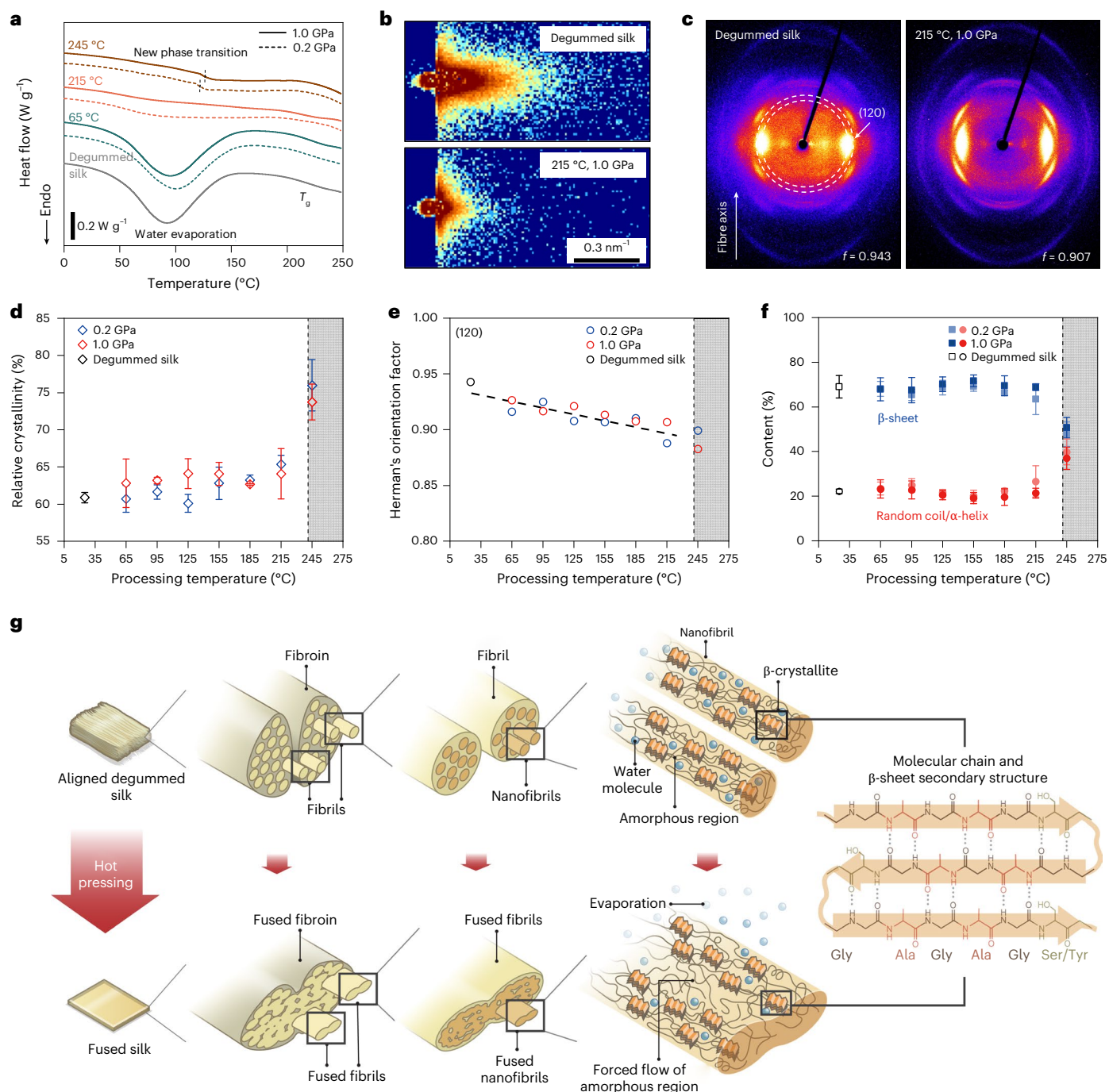


Fig. 2 | Retention of the complex hierarchical organization. **a**, DSC curves of degummed silk and fused silk fabricated under different processing conditions. **b, c**, 2D SAXS patterns (**b**) and WAXS patterns (**c**) of degummed silk and fused silk fabricated at 215 °C and 1.0 GPa. **d**, Relative crystallinity of degummed silk and fused silk fabricated at different processing conditions, calculated from one-dimensional wide-angle X-ray diffraction profiles. Data are presented as mean \pm s.d. ($n = 3$ independent samples). **e**, Herman's orientation factor of the crystal plane (120), from 2D WAXS results. **f**, Content of protein secondary structures (β -sheet and random coil/ α -helix) in degummed silk and fused

silk materials fabricated at different conditions, from FTIR spectra. Data are presented as mean \pm s.d. ($n = 3$ independent samples). The shaded area in **d**, **e** and **f** highlights the samples processed within this high temperature region, where silk undergoes severe thermal degradation. This degradation alters the amorphous phase and generates degradation products, leading to apparent increases in relative crystallinity and artificial shifts in FTIR-derived secondary structure content. **g**, Schematic of the mechanism of self-diffusion during the hot-pressing process.

21.5 \pm 0.3 GPa and, importantly, tensile toughness of 45 \pm 3 MJ m⁻³ are demonstrated, surpassing those of bone and polycarbonate and approaching those of Kevlar fibres (Supplementary Fig. 12). In the flexural tests, low processing temperatures (95–155 °C) resulted in weak interfibre bonding, leading to poor load transfer, reduced flexural modulus and strength, and shear failure in the interfibre regions. Processing

at 185 °C and 215 °C enhanced the self-diffusion of silk fibres, improving load transfer and resulting in more typical flexural failure, substantially increasing flexural modulus and strength. As expected, excessively high temperatures (245 °C) caused severe thermal degradation and diminished flexural properties. Both the tensile curves (Fig. 3b) and finite element simulations (Fig. 3e and Supplementary Fig. 14) further

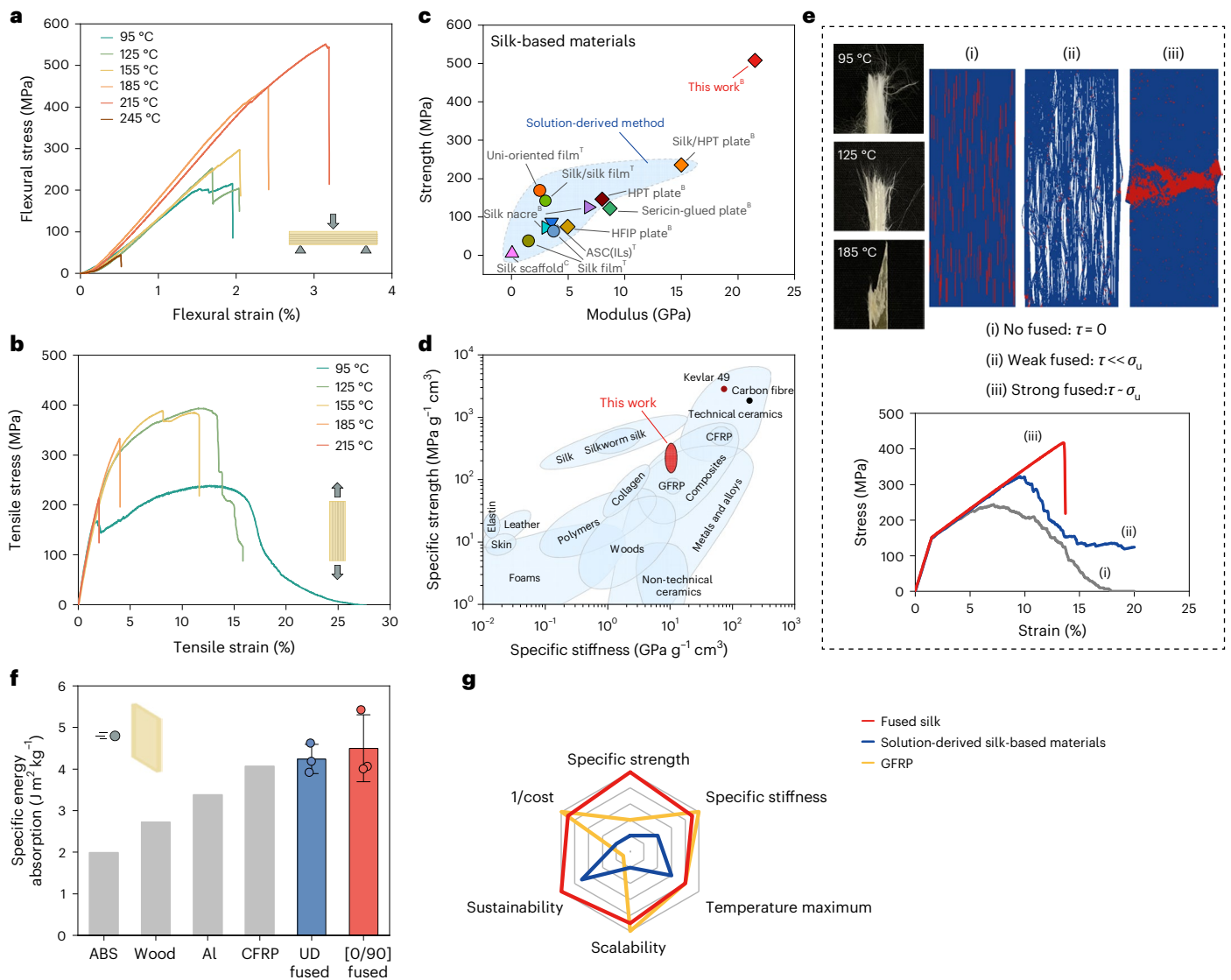


Fig. 3 | Remarkable mechanical properties. **a**, Three-point bending curves for fused silk fabricated at different temperatures and 0.2 GPa. **b**, Tensile curves for fused silk fabricated at different temperatures and 0.2 GPa. **c**, Comparison of strength and modulus of fused silk and silk-based materials reported in the scientific literature. B, bending test; C, compression test; T, tensile test (Supplementary Table 2). **d**, Ashby plot comparing the specific stiffness and strength of fused silk with other natural and synthetic materials^{27,47}. **e**, Finite element simulation of fused silk with varying strengths of fusion. Red elements denote failed regions; blue elements represent intact areas. The accompanying

photographs show tensile fracture cross-sections of fused silk fabricated at 95 °C, 125 °C and 185 °C under 0.2 GPa. The stress-strain curves predicted by the simulations illustrate the mechanical responses of fused silk with different fusion strengths. **f**, Comparison of ballistic specific energy absorption of UD and [0/90] fused silk materials with widely used materials: ABS, Al and CFRP. Data are presented as mean \pm s.d. ($n = 3$ independent specimens for fused silk materials). **g**, A comparison of the performance of fused silk, solution-derived silk-based materials and GFRP composites (Supplementary Table 7).

demonstrated the impact of fibroin interlinking on tensile behaviour. The simulation results indicated that, without altering the axial properties of the fibres, higher interfibre adhesion strength increased tensile strength in the UD model but shifted the fracture mode from ductile to brittle³⁶. Good agreement was observed between computational simulations and tensile curves at low processing temperatures (95–155 °C). At 185 °C and 215 °C, the tensile strength of the materials decreased, showing a brittle failure mode. Taking into account also the flexural test results, we attribute this behaviour to the reduced axial properties of silk fibres, caused by a slight thermal degradation^{33,37}, decreased orientation of β -crystallite and an increased sensitivity to internal voids or microcracks at higher degrees of fusion.

The mechanical properties of fused silk fabricated using this method are not only remarkably superior to those reported previously

for any silk-based material (mostly obtained via solution) (Fig. 3c) but also exceed those of many currently widely used structural materials such as woods and GFRP (Fig. 3d). Single-edge notched bending (SENB) tests of fused silk show a surprising combination of high strength (380 ± 30 MPa) and fracture toughness (20 ± 2 MPa m^{1/2}), two typically mutually exclusive properties (Supplementary Fig. 15). In addition to the exceptional quasistatic mechanical properties, a ballistic test was used to evaluate the high-speed impact mechanical properties. UD and [0/90] fused silk demonstrated excellent impact resistance, with a specific energy absorption reaching 4.5 ± 0.7 J m² kg⁻¹, higher than CFRP (Fig. 3f and Supplementary Fig. 16). A further embodiment derived from the thermal and thermodynamic analyses, which indicated a consistent glass-transition temperature of fused silk at -219 °C (Fig. 2a and Supplementary Fig. 17). As a result, fused silk can

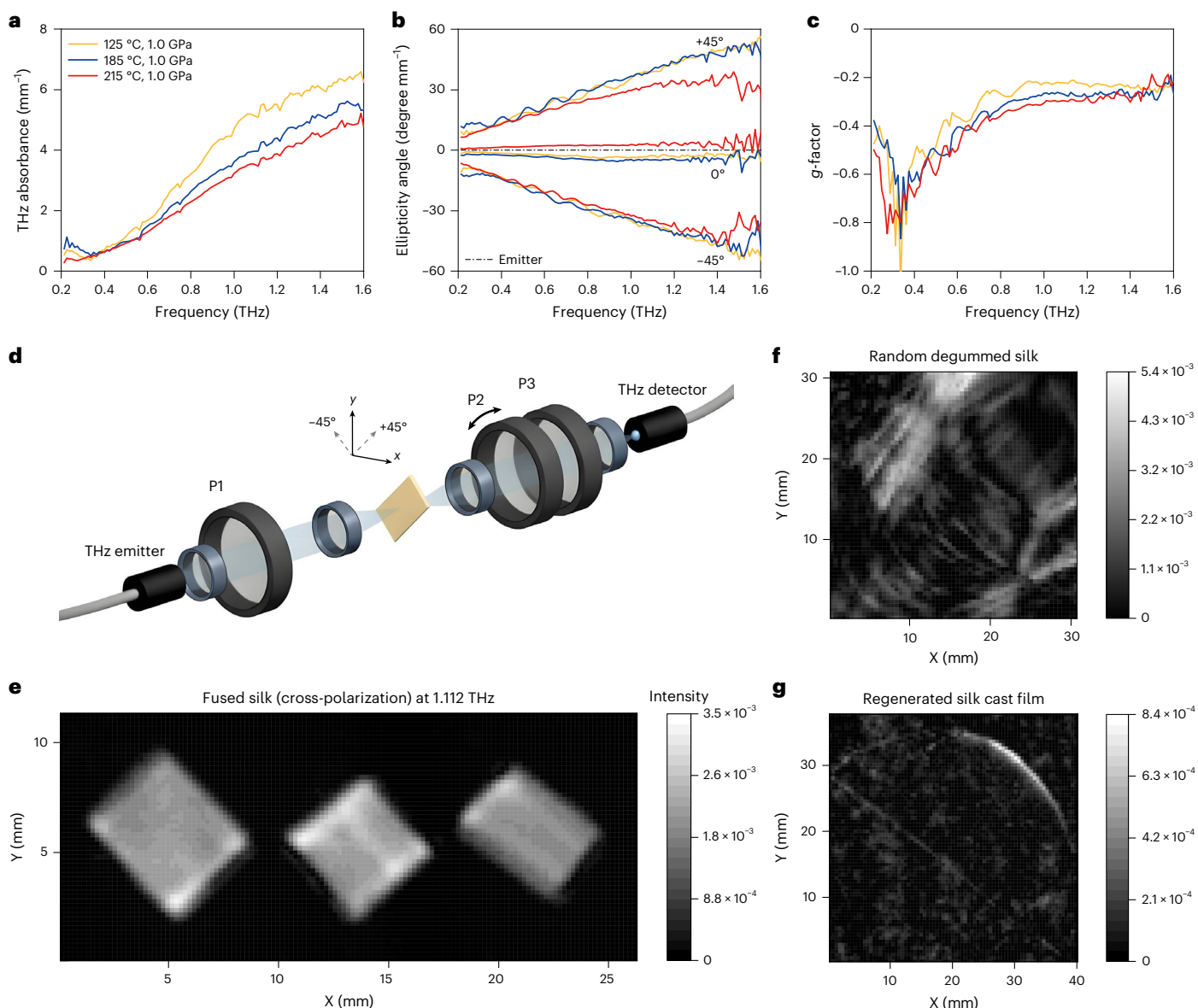


Fig. 4 | Giant THz optical response. **a**, THz absorbance spectra (normalized by thickness) of fused silk fabricated at different temperatures and 1.0 GPa. **b**, Polarization ellipticity angle after incident THz linear polarization transmitted through the three fused silk specimens. **c**, Calculated g -factor of the three

specimens in the THz regime. **d**, THz-TDP setup. P1, P2 and P3 indicate the first, second and third polarizers. **e–g**, THz cross-polarization state images for the fused silk (**e**, from left to right: 95 °C, 0.2 GPa; 125 °C, 1.0 GPa; and 185 °C, 1.0 GPa), random degummed silk (**f**) and regenerated silk cast film (**g**).

be thermoformed or repaired by heating around the glass-transition temperature, an increasingly vital feature for sustainable materials (Supplementary Fig. 18). Further exploratory experiments demonstrate the universal applicability of our simple thermomechanical approach for forming fused silk with exceptional performance from different silk fibre sources, including spider (*Trichonephila inaurata* dragline) silk and end-of-life silk textiles (Extended Data Fig. 3).

Fused silk possesses desirable characteristics such as easy and scalable manufacturability, sustainability and biodegradability and mechanical properties on par with high-performance structural materials (Fig. 3g), which makes them ideal structural materials for various application fields.

Giant THz optical response

The unique optical properties of the fused silk are not limited to the visible range. This material exhibits exceptionally intense THz polarization activity that exceeds that of cast-and-dry film (that

is, regenerated silk film), dense dispersions and original fibres (Fig. 4), where the THz optical properties were obtained with THz time-domain polarimetry (THz-TDP) (Fig. 4d). Fused silk exhibits a broad increase in THz absorbance at higher frequency, which is typical for dielectric materials (Fig. 4a). No distinct peaks appear in the THz absorbance spectra, indicating that the fused silk lacks intrinsic resonances in the THz regime. Owing to the intrinsic fibrous alignment of silk fibres, fused silk demonstrates linear birefringence arising from their anisotropic structural organization. This directional optical anisotropy induces polarization-dependent phase retardation, leading to strong modulation of the transmitted polarization state (Supplementary Fig. 20). Notably, the birefringent response leads to high polarization ellipticity when linearly polarized THz waves propagate through the material (Fig. 4b and Supplementary Fig. 21). All samples exhibit similar normalized ellipticity spectra across the THz frequency range, enabling precise polarization control through modulation of material thickness. The strong THz polarization

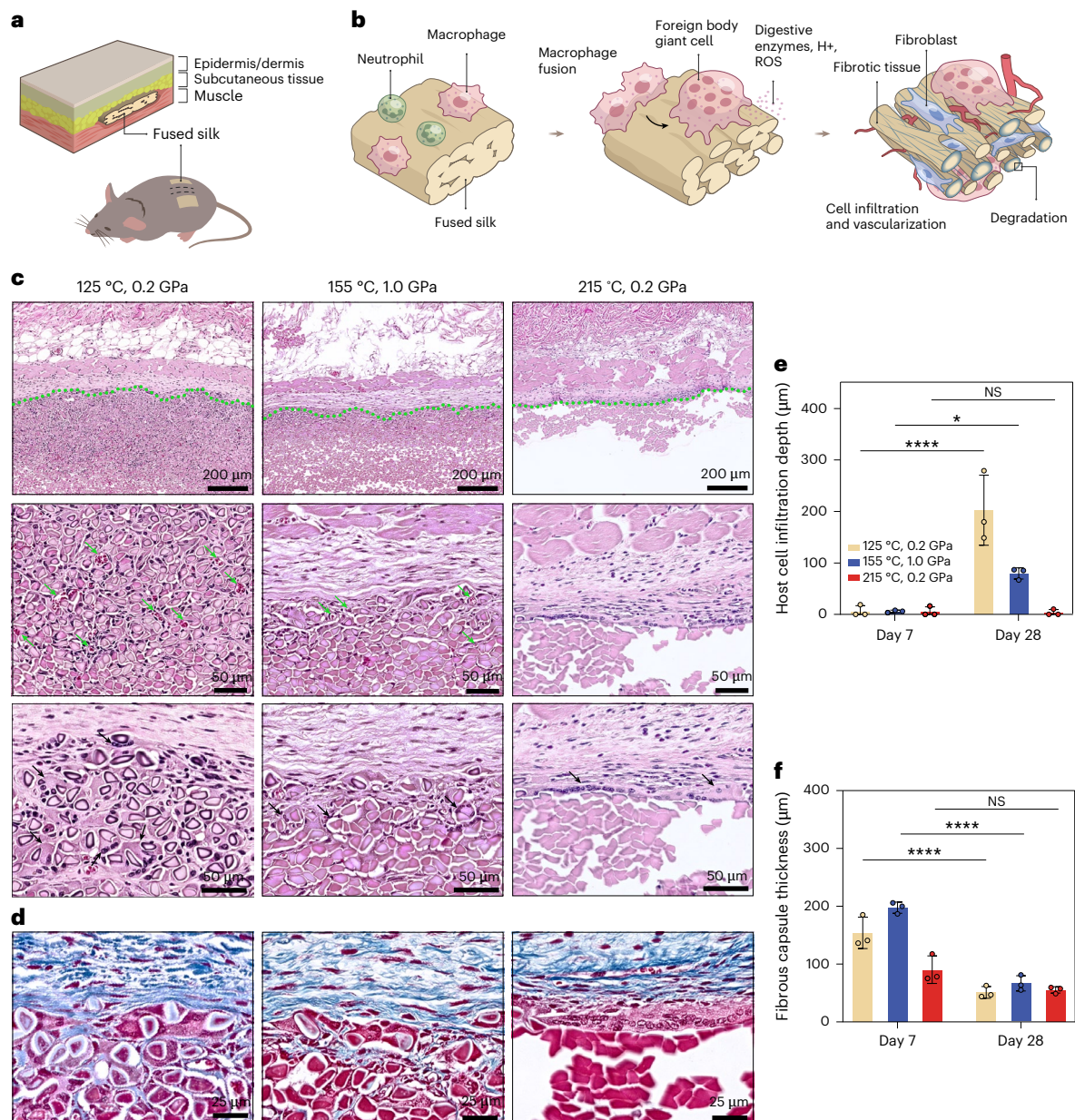


Fig. 5 | Biocompatibility and biodegradability. **a**, Schematic illustrating the subcutaneous implantation of fused silk. **b**, Schematic illustrating host response to fused silk, including possible cellular infiltration, tissue integration and material degradation over time. ROS, reactive oxygen species. **c**, Representative histology images of the H&E staining of fused silk prepared at three different conditions (125 °C, 0.2 GPa; 155 °C, 1.0 GPa; and 215 °C, 0.2 GPa) after 28 days of implantation. Green-dashed lines indicate the implant–tissue interface; green arrows indicate blood vessels; black arrows indicate foreign body giant cells. **d**, Representative images of the MT staining of the fused silk after 28 days of subcutaneous implantation prepared at three different conditions (125 °C, 0.2 GPa; 155 °C, 1.0 GPa; and 215 °C, 0.2 GPa). **e**, The depth of host cell infiltration

into the implant after 7 days and 28 days of subcutaneous implantation based on H&E staining ($n = 3$ biological independent replicates, $P < 0.0001$ (125 °C, 0.2 GPa, day 7 versus day 28), $P = 0.0259$ (155 °C, 1.0 GPa, day 7 versus day 28), $P = 0.9997$ (215 °C, 0.2 GPa, day 7 versus day 28)). **f**, Fibrous capsule thickness at the implant–tissue interface was measured after 7 days and 28 days of subcutaneous implantation based on MT staining ($n = 3$ biological independent replicates, $P < 0.0001$ (125 °C, 0.2 GPa, day 7 versus day 28), $P < 0.0001$ (155 °C, 1.0 GPa, day 7 versus day 28), $P = 0.0764$ (215 °C, 0.2 GPa, day 7 versus day 28)). All data are represented as means \pm s.d. Statistical significance was determined using two-way ANOVA with Sidak’s multiple comparisons. * $P < 0.05$, ** $P < 0.01$, *** $P < 0.001$, **** $P < 0.0001$; NS, not significant.

rotation is further supported by their g -factor values (Fig. 4c), reaching nearly -1 at low frequencies and maintaining values between -0.2 and -0.35 at higher frequencies, which represents the current record for THz chiral optics and is approaching to the theoretical limit of $g = 2.0$.

Confirmation of the uniquely high polarization rotation of fused silk prepared in a form factor convenient for optical devices can be obtained by THz cross-polarization imaging at 1.112 THz (Fig. 4f,g and

Supplementary Figs. 22 and 23). To achieve maximum transmission under the cross-polarization condition, where the orientation of the second polariser was at 0° , silk-based samples were oriented at 45° with respect to the incident THz polarization (Fig. 4d). Fused silk (Fig. 4e) and degummed silk fibres (Fig. 4f) are distinctly visible under cross-polarization. In contrast, regenerated silk cast film (Fig. 4g), which lacks both structural alignment and sufficient crystallinity, exhibits negligible contrast under the same condition.

Biocompatibility and biodegradability

In vivo biocompatibility and biodegradability of the fused silk was assessed through subcutaneous implantation in C57BL/6 mice for 4 weeks (Fig. 5a). Silk materials typically elicit a mild inflammatory reaction that subsides within a few weeks^{38,39}. Depending on the implant properties and implant site, the host response to silk may involve recruitment and activation of macrophages, as well as the initiation of a mild foreign body reaction characterized by the formation of multinucleated giant cells (MNGCs)^{40,41}. Figure 5b provides a schematic illustration of the host response to the fused silk material. After 7 days of implantation, minimal host cell infiltration and tissue ingrowth was observed across all implant types (Fig. 5e and Extended Data Fig. 4). By 28 days post-implantation, a significant increase in host cell infiltration was noted in the 125 °C, 0.2 GPa and 155 °C, 1.0 GPa implants (Fig. 5c,e). By contrast, the 215 °C, 0.2 GPa implant showed negligible host cell infiltration and tissue ingrowth at day 28 (Fig. 5c,d and Supplementary Fig. 25), probably due to stronger interfibre fusion, reducing accessibility to host cells. Masson's trichrome (MT) staining revealed a significant decrease in the thickness of the collagenous fibrous capsule surrounding the 125 °C, 0.2 GPa and 155 °C, 1.0 GPa implants from day 7 to day 28 (Fig. 5f), indicating a diminishing inflammatory response. Conversely, the fibrous capsule thickness around the 215 °C, 0.2 GPa implant remained relatively stable from day 7 to day 28, potentially indicating a more inert interface, favourable for long-term stability.

Owing to its high β -sheet content and dense structure, fused silk is expected to degrade slowly in vivo. Immune cells, particularly macrophages and MNGCs, play a primary role in silk degradation in vivo⁴². MNGCs were detected at the implant–tissue interface as early as day 7 across all implant types (Extended Data Fig. 4). By day 28, MNGCs were observed both at the implant–tissue interface and within the 125 °C, 0.2 GPa and 155 °C, 1.0 GPa implants, while MNGCs were only found at the implant–tissue interface in 215 °C, 0.2 GPa implant (Fig. 5d). The higher number and deeper infiltration of MNGCs in the 125 °C, 0.2 GPa implants suggest more extensive degradation at day 28. Additionally, silk fibres near the implant–tissue interface exhibited increased blue staining (Fig. 5d), indicating in vivo silk degradation⁴³. These degradation patterns align with enzyme-mediated in vitro results (Extended Data Fig. 5). Moreover, MNGC presence within the 125 °C and 155 °C implants correlated with enhanced vascularization (Fig. 5c), consistent with previous findings that MNGCs release pro-angiogenic signals such as VEGF⁴⁴. In summary, fused silk demonstrated biocompatibility, with a degradation and host response which can be tuned through processing conditions, supporting their potential for use in biomedical applications requiring controlled degradation and tissue integration.

Discussion

The simple thermomechanical strategy proposed here enables the fabrication of fused silk solely by applying heat and pressure and it demonstrates broad generality across different silk sources, ranging from *B. mori* silk to *T. inaurata* spider dragline silk. Compared with traditional solution-derived methods, this purely physical process enables higher yield, lower energy consumption and shorter processing time, while avoiding chemical usage and associated liquid waste, without compromising the intrinsic structural advantages of silk. This shift towards a solvent-free, thermomechanical route may open new possibilities for the scalable manufacturing of silk-based materials. Importantly, fused silk retains biodegradability and biocompatibility while exhibiting remarkable mechanical properties and record-high chiroptical activity in the THz range that silk fibres, regenerated silk or other materials cannot achieve. These characteristics point towards broader potential for fused silk as a promising platform for sustainable, high-performance and multifunctional materials, with future prospects spanning lightweight engineering structures, optically active THz components and biodegradable high-performance medical implants, as well as the upcycling of waste silk into value-added products.

Methods

Materials

Commercial reeled *B. mori* silk was bought from George Weil & Sons, UK. *Antheraea pernyi* and *Samia ricini* silk tops were bought from Wild Fibres, UK. *T. inaurata* spider dragline silk was collected at Medical University of Vienna. Na₂CO₃ (Acros Organics, 123670010) and deionized water were used for degumming the silk. Natural wood, acrylonitrile butadiene styrene (ABS) (Filamentive, 1006555), aluminium film and carbon fibre/epoxy resin composites (CFRP) were used for ballistic tests.

Fabrication of fused silk

Commercial *B. mori* reeled silk was immersed in a 95 °C aqueous 0.02 M Na₂CO₃ solution for 30 min twice to remove the sericin and then washed in deionized water several times to remove the residual Na₂CO₃ and sericin. The degummed silk was then aligned along the fibre direction after immersion in water and fixed at both ends in a square stainless-steel frame to prevent shrinkage and distortion. Afterwards, the degummed silk was dried in an oven at 45 °C overnight and stored in ambient conditions. Before hot-pressing, the dry degummed silk was removed from the frame and cut to the required sizes with a knife. To prevent samples from sticking on the aluminium moulds, PTFE mould release was sprayed on the surface of the mould (optional, only at 245 °C processing temperature, samples stuck to the mould). For the UD samples, the aligned silk fibres were put into moulds, hot-pressing with a COLLIN P300E Press for 5 min at different processing pressures and temperatures and then cooled to room temperature under pressure. For [0/90] samples, two layers of aligned silk fibres were stacked together in the 0° and 90° directions and then hot-pressed in the same way.

Mechanical tests

The three-point bending, tensile and SENB tests were performed on a universal mechanical testing machine, Instron 5900R84, equipped with a 1-kN load cell. All tests were conducted at room temperature and ~45% relative humidity and the specimens at dry state were subjected to a constant loading rate of 2 mm min⁻¹. The dimensions of three-point bending specimens were about 16 mm in length, 5 mm in width and 0.6 mm in thickness. The support lengths were determined on the basis of the thickness of the specimens, with a span-to-depth ratio of 16 as specified by the ASTM D790. The tensile specimens had dimensions of about 35 mm in length, 3 mm in width and 0.6 mm in thickness, with a gauge length of 20 mm. The SENB specimens were the same size as the three-point bending specimens and were notched to approximately half their thickness using a sharp blade (refer to ASTM E1820).

Finite element analysis

Fused silk materials were modelled by a commercial finite element package ABAQUS 2022 as a bundle of silk fibres with a size of 1,500 × 4,000 μm². In this model, 150 individual silk fibres with 200 elements in a single silk fibre were built (Supplementary Fig. 14). A bilinear elastic-plastic model was used in silk materials by a user-defined field (USDFLD) subroutine and the strength of each silk fibre element was assigned to follow the power law-accelerated Weibull distribution:

$$P(\sigma_u) = 1 - \exp \left[- \left(\frac{l_e}{L_0} \right)^\alpha \left(\frac{\sigma_u}{\sigma_0} \right)^\rho \right] \quad (1)$$

where l_e is the element size, L_0 is the reference gauge length, σ_u is the element strength and α , ρ and σ_0 are parameters of the power law-accelerated Weibull distribution. All parameters were obtained from single silk fibre tensile tests. A zero-thickness cohesive zone with a bilinear traction-separation law was inserted between the silk fibres to simulate the bonding behaviour. The tensile behaviour of fused silk with different bounding strengths was simulated by applying a constant strain of 0.2.

Ballistic test

The ballistic tests on different materials were performed using a Sydor technologies high-velocity impact testing system. A single-stage gas gun was driven by compressed air to accelerate steel balls with a diameter of 7 mm (1.4 g in mass) as projectiles to impact the specimens. An aluminium fixture with a 30-mm side-length square hole held specimens vertically against the support frame. The impact process was recorded by a high-speed camera, Photron FASTCAM Nova S9, which was set on the side of the test machine. Two light gates were installed on the trajectory to measure the initial velocity and the residual velocity was obtained using the software PFV4 from Photron company. The specific energy absorption e_s was calculated using the following equation:

$$e_s = \frac{\frac{1}{2}m_p(v_i^2 - v_r^2)}{A} \quad (2)$$

where m_p is the mass of the projectile, v_i and v_r are the initial and residual velocities of the projectile and A is the area density of the specimen.

Thermal analysis

The thermal degradation of the degummed silk was measured by a TA Instruments TGA 5500 with a heating rate of $10\text{ }^\circ\text{C min}^{-1}$ in nitrogen or air atmosphere from room temperature to $600\text{ }^\circ\text{C}$. DSC measurements were carried out on a TA Instruments DSC 25 with a heating rate of $10\text{ }^\circ\text{C min}^{-1}$ in nitrogen gas flow of 25 ml min^{-1} from $-50\text{ }^\circ\text{C}$ to $300\text{ }^\circ\text{C}$. Dynamic mechanical analysis measurements were performed on a TA Instruments RSA-G2 using a single cantilever mode. The specimens were about 15 mm in length, 5 mm in width and 0.6 mm in thickness. The tests were carried out from room temperature to $250\text{ }^\circ\text{C}$ with a temperature ramp rate of $3\text{ }^\circ\text{C min}^{-1}$, a frequency of 1 Hz and a dynamic strain of 0.2%.

FTIR spectroscopy

The FTIR measurements were carried out using a Bruker Tensor 27 spectrometer fitted with a platinum attenuated total reflectance diamond accessory. The spectrum was recorded with 32 scans and a resolution of 4 cm^{-1} in the wavenumber range of $4,000\text{--}400\text{ cm}^{-1}$. The thickness of fused silk samples was $\sim 0.6\text{ mm}$. Gaussian fitting was used to deconvolute all the protein secondary structure peaks of the amide I region ($1,720\text{--}1,580\text{ cm}^{-1}$) using the PeakFit 4.12 software. Four primary peaks were assigned to the protein secondary structures: β -sheet ($1,618\text{ cm}^{-1}$ and $1,698\text{ cm}^{-1}$), random coil/ α -helix ($1,645\text{--}1,655\text{ cm}^{-1}$) and β -turn ($1,685\text{ cm}^{-1}$). All the coefficients of determinations (R^2) for the deconvolution were greater than or equal to 0.99.

X-ray diffraction/scattering

One-dimensional wide-angle X-ray diffraction (WAXD) measurements of degummed silk and fused silk were performed using a $\text{CuK}\alpha$ ($\lambda = 0.1541\text{ nm}$) source PANalytical X'Pert Pro diffractometer in reflection mode. PeakFit 4.12 software was used to calculate relative crystallinity. The 2D WAXS patterns for calculating crystal orientation were collected using a $\text{CuK}\alpha$ source Rigaku RAPID II instrument equipped with a curved 2D detector in transmission mode. An exposure time of 60 min was used for all silk samples at ambient conditions. The 2D SAXS patterns were collected using a $\text{CuK}\alpha$ source PANalytical Empan diffractometer with a ScatterX78 attachment and a PIXcel3D detector under low vacuum conditions for 5,000 s (1,000 s for quick tests) exposure. One sample ($n = 1$) was measured for each condition in 2D WAXS and 2D SAXS measurements.

Scanning electron microscopy

Hitachi S-3700N and FEI Inspect F scanning electron microscopes were used to characterize the morphologies of the silk materials with a voltage of 5 kV. The surfaces of the specimens were sputter coated with a thin layer of gold by an AGAR auto sputter coater.

THz-TDP setup

To measure the THz polarization activity of fused silk materials, THz-TDP was used. A conventional THz-TDS (TeraSmart, Menlo Systems) was used for generation and detection of the THz pulse, which consists of photoconductive antennas (Tera15-FC, Menlo Systems) as emitter and detector, a pulsed laser at $1,560\text{ nm}$ and four identical convex lenses (TPX50, Menlo Systems) for collimating and focusing the THz beam. A motorized XY stage accomplished sample scanning and imaging in the THz focal plane. Unlike conventional THz-TDS, three home-made linear polarizers were added for determination of the THz rotation angle (θ) and ellipticity angle (η) of the measured sample. For such polarization measurement, the antenna direction of the emitter was fixed to the horizontal orientation (x axis) to the optical table where the detector was aligned to the vertical orientation (y axis), being in a cross-polarization state. The first (P1) and third (P3) polarizers were placed right in front of the emitter and detector with the same alignment direction, respectively. The second (P2) polarizer was placed between P1 and P3 and was rotated to three different orientations ($+45^\circ$, 0° and -45° where the angle is measured with respect to the y axis) during the measurements.

When P2 axis is at 0° , the measured THz pulse is the transmitted pulse under cross-polarization state, where we define the time-domain THz pulse as $E_y(t)$. The x -component is extracted by rotating the P2 axis to $+45^\circ$ ($E_{+45^\circ}(t)$) and -45° ($E_{-45^\circ}(t)$) and subtracting the measured THz pulses.

$$E_x(t) = E_{+45^\circ}(t) - E_{-45^\circ}(t) \quad (3)$$

For frequency-domain analysis, fast Fourier transform (FFT) was conducted to the measured time-domain electric fields as follows:

$$\tilde{E}_x = \tilde{E}_x(\omega) = \text{FFT}\{E_x(t)\} \quad (4)$$

$$\tilde{E}_y = \tilde{E}_y(\omega) = \text{FFT}\{E_y(t)\} \quad (5)$$

The transmitted spectra of the sample (fused silk materials) and the reference (air) then can be calculated as:

$$T_s = \sqrt{|\tilde{E}_x|^2 + |\tilde{E}_y|^2} \quad (6)$$

$$T_{\text{ref}} = \sqrt{|\tilde{E}_{x,\text{ref}}|^2 + |\tilde{E}_{y,\text{ref}}|^2} \quad (7)$$

On the basis of the transmittance spectra, the THz absorbance (TA) can be calculated by:

$$\text{TA} = -\ln\left(\frac{T_s}{T_{\text{ref}}}\right) \quad (8)$$

To obtain the THz polarization activity spectra, Stokes equations were exploited, where they are defined as:

$$S_0 = \tilde{E}_x\tilde{E}_x^* + \tilde{E}_y\tilde{E}_y^* \quad (9)$$

$$S_1 = \tilde{E}_x\tilde{E}_x^* - \tilde{E}_y\tilde{E}_y^* \quad (10)$$

$$S_2 = \tilde{E}_x\tilde{E}_y^* + \tilde{E}_y\tilde{E}_x^* \quad (11)$$

$$S_3 = i(\tilde{E}_x\tilde{E}_y^* - \tilde{E}_y\tilde{E}_x^*) \quad (12)$$

We can then calculate the rotation angle (θ) and ellipticity angle (η) as:

$$\theta = \frac{1}{2} \tan^{-1}\left(\frac{S_2}{S_1}\right) \quad (13)$$

$$\eta = \frac{1}{2} \sin^{-1}\left(\frac{S_3}{S_0}\right) \quad (14)$$

For the imaging under cross-polarization, the axis of P2 was aligned at 0° and the sample was imaged with the motorized XY stage. The imaged results show the transmitted intensity of the THz at a certain frequency.

Subcutaneous implantation and histology

The animal study was reviewed and approved by the Institutional Animal Care and Use Committee of Tufts University (animal protocol M2022-121). Mice (five mice per cage) were housed in a specific pathogen-free environment at a temperature of 18–22 °C and a humidity of 50–60%, with a dark/light cycle of 12 h. All mice were promptly euthanized using CO₂ gas after finishing animal experiment. Samples were sterilized by ethylene oxide before implantation. Eight-week-old C57BL/6 mice (Charles River Laboratories International) were anaesthetized with 3–5% isoflurane in oxygen for induction and 1–3% for maintenance. Buprenorphine-SR (1.0 mg kg⁻¹) was administered subcutaneously as an analgesic before surgery. The dorsal hair was shaved and a 1-cm longitudinal incision was made on the skin on each side of the spine using surgical scissors to access the subcutaneous space. Then subcutaneous pockets were created with blunt forceps for the implantation of the silk samples ($n = 3$). After implantation, the incisions were closed using wound clips. Each animal received two implants from two different study groups. The animals were euthanized by CO₂ asphyxiation and cervical dislocation and silk samples together with the surrounding tissue were excised and collected at 7 days and 28 days post-implantation. The explanted samples were fixed in 4% paraformaldehyde and embedded in paraffin for histological analysis. Sections with a thickness of 5 μm were obtained by sectioning the explant along either the transverse or longitudinal axes of the silk fibres. The sections were deparaffinized in xylene, rehydrated through an ethanol gradient and subsequently stained with haematoxylin and eosin (H&E) for cellularity and Masson's trichrome (MT) for collagen according to standard histological protocols. Histology images were acquired using Thermofisher Scientific EVOS M7000 Imaging System (7 days) and Grindium Inc Ocus 40 Digital Microscope Slide Scanner (28 days). Host cell infiltration depth and the fibrous capsule thickness were quantified using ImageJ 1.54 g software.

Statistical analysis

GraphPad Prism 9 was used for all statistical analysis and all data are shown as mean ± s.d. Statistical significance was determined using two-way analysis of variance (ANOVA) with Sidak's multiple comparisons. Values with $P < 0.05$ were considered statistically significant ($*P < 0.05$, $**P < 0.01$, $***P < 0.001$, $****P < 0.0001$; NS, not significant).

Reporting summary

Further information on research design is available in the Nature Portfolio Reporting Summary linked to this article.

Data availability

All data that support the findings of this study are available in the paper and Supplementary Information. Source data are provided with this paper.

Code availability

The ABAQUS USDFLD subroutine used to implement the stochastic strength field in the finite element analysis of fused silk is available via Zenodo at <https://doi.org/10.5281/zenodo.18775588> (ref. 45). The custom code used for the silk THz experiments is available via Zenodo at <https://doi.org/10.5281/zenodo.18688272> (ref. 46).

References

- Vollrath, F. & Knight, D. P. Liquid crystalline spinning of spider silk. *Nature* **410**, 541–548 (2001).
- Shao, Z. & Vollrath, F. Surprising strength of silkworm silk. *Nature* **418**, 741–741 (2002).
- Ling, S., Kaplan, D. L. & Buehler, M. J. Nanofibrils in nature and materials engineering. *Nat. Rev. Mater.* **3**, 18016 (2018).
- Perea, G. B. et al. The apparent variability of silkworm (*Bombyx mori*) silk and its relationship with degumming. *Eur. Polym. J.* **78**, 129–140 (2016).
- Altman, G. H. et al. Silk-based biomaterials. *Biomaterials* **24**, 401–416 (2003).
- Guo, C., Li, C. & Kaplan, D. L. Enzymatic degradation of *Bombyx mori* silk materials: a review. *Biomacromolecules* **21**, 1678–1686 (2020).
- Meyers, M. A., McKittrick, J. & Chen, P.-Y. Structural biological materials: critical mechanics–materials connections. *Science* **339**, 773–779 (2013).
- Craig, C. L. *Spiderwebs and Silk: Tracing Evolution From Molecules to Genes to Phenotypes* (Oxford Univ. Press, 2003).
- Babb, P. L. et al. The *Nephila clavipes* genome highlights the diversity of spider silk genes and their complex expression. *Nat. Genet.* **49**, 895–903 (2017).
- Omenetto, F. G. & Kaplan, D. L. New opportunities for an ancient material. *Science* **329**, 528–531 (2010).
- Blamires, S. J., Blackledge, T. A. & Tso, I.-M. Physicochemical property variation in spider silk: ecology, evolution, and synthetic production. *Annu. Rev. Entomol.* **62**, 443–460 (2017).
- Wang, Y. et al. Silk-protein-based gradient hydrogels with multimode reprogrammable shape changes for biointegrated devices. *Proc. Natl Acad. Sci. USA* **120**, e2305704120 (2023).
- Candido, I. C. et al. PVA-silk fibroin bio-based triboelectric nanogenerator. *Nano Energy* **105**, 108035 (2023).
- Han, Y. et al. Design of biodegradable, climate-specific packaging materials that sense food spoilage and extend shelf life. *ACS Nano* **17**, 8333–8344 (2023).
- Wang, H. et al. Inter-shell sliding in individual few-walled carbon nanotubes for flexible electronics. *Adv. Mater.* **35**, 2306144 (2023).
- Qiu, W., Patil, A., Hu, F. & Liu, X. Y. Hierarchical structure of silk materials versus mechanical performance and mesoscopic engineering principles. *Small* **15**, 1903948 (2019).
- Wang, Q. et al. Observations of 3 nm silk nanofibrils exfoliated from natural silkworm silk fibers. *ACS Mater. Lett.* **2**, 153–160 (2020).
- Li, C. et al. Fiber-based biopolymer processing as a route toward sustainability. *Adv. Mater.* **34**, 2105196 (2022).
- Cebe, P. et al. Beating the heat-fast scanning melts silk beta sheet crystals. *Sci. Rep.* **3**, 1130 (2013).
- Zhang, X., Ries, M. E. & Hine, P. J. Time–temperature superposition of the dissolution of silk fibers in the ionic liquid 1-ethyl-3-methylimidazolium acetate. *Biomacromolecules* **22**, 1091–1101 (2021).
- Zhang, X., Ries, M. E. & Hine, P. J. Dissolution dynamics of woven all-silk composites fabricated in the ionic liquid 1-ethyl-3-methylimidazolium acetate. *Compos. Sci. Technol.* **239**, 110046 (2023).
- Liu, Y. et al. Biomimetic silk architectures outperform animal horns in strength and toughness. *Adv. Sci.* **10**, 2303058 (2023).
- Rockwood, D. N. et al. Materials fabrication from *Bombyx mori* silk fibroin. *Nat. Protoc.* **6**, 1612–1631 (2011).
- Koh, L.-D. et al. Structures, mechanical properties and applications of silk fibroin materials. *Prog. Polym. Sci.* **46**, 86–110 (2015).
- Reizabal, A., Costa, C. M., Pérez-Álvarez, L., Vilas-Vilela, J. L. & Lanceros-Méndez, S. Silk fibroin as sustainable advanced material: material properties and characteristics, processing, and applications. *Adv. Funct. Mater.* **33**, 2210764 (2023).
- Guo, C. et al. Thermoplastic moulding of regenerated silk. *Nat. Mater.* **19**, 102–108 (2020).
- Ashby, M. F. *Materials Selection in Mechanical Design* 4 edn (Butterworth-Heinemann, 2011).
- Yang, Z., Grubb, D. & Jelinski, L. Small-angle X-ray scattering of spider dragline silk. *Macromolecules* **30**, 8254–8261 (1997).

29. Yoshioka, T., Tsubota, T., Tashiro, K., Jouraku, A. & Kameda, T. A study of the extraordinarily strong and tough silk produced by bagworms. *Nat. Commun.* **10**, 1469 (2019).
30. Magoshi, J. & Nakamura, S. Studies on physical properties and structure of silk. Glass transition and crystallization of silk fibroin. *J. Appl. Polym. Sci.* **19**, 1013–1015 (1975).
31. Cho, S. Y. et al. Carbonization of a stable β -sheet-rich silk protein into a pseudographitic pyroprotein. *Nat. Commun.* **6**, 7145 (2015).
32. Hashimoto, T., Taniguchi, Y., Kameda, T., Tamada, Y. & Kurosu, H. Changes in the properties and protein structure of silk fibroin molecules in autoclaved fabrics. *Polym. Degrad. Stabil.* **112**, 20–26 (2015).
33. Martel, A., Burghammer, M., Davies, R. & Riekel, C. Thermal behavior of *Bombyx mori* silk: evolution of crystalline parameters, molecular structure, and mechanical properties. *Biomacromolecules* **8**, 3548–3556 (2007).
34. Sahu, V. et al. Heavily nitrogen doped, graphene supercapacitor from silk cocoon. *Electrochim. Acta* **160**, 244–253 (2015).
35. Latza, V. et al. Multi-scale thermal stability of a hard thermoplastic protein-based material. *Nat. Commun.* **6**, 8313 (2015).
36. Perez-Rigueiro, J., Herrero, P. & Llorca, J. Identification of weak interfaces in composites using transmission electron microscopy. *J. Microsc.* **197**, 202–205 (2000).
37. Lee, J. H. et al. Preparation of new natural silk non-woven fabrics by using adhesion characteristics of sericin and their characterization. *Int. J. Biol. Macromol.* **106**, 39–47 (2018).
38. Li, C. et al. Design of biodegradable, implantable devices towards clinical translation. *Nat. Rev. Mater.* **5**, 61–81 (2020).
39. Thurber, A. E., Omenetto, F. G. & Kaplan, D. L. In vivo bioresponses to silk proteins. *Biomaterials* **71**, 145–157 (2015).
40. Ghanaati, S. et al. Fine-tuning scaffolds for tissue regeneration: effects of formic acid processing on tissue reaction to silk fibroin. *J. Tissue Eng. Regen. Med.* **4**, 464–472 (2010).
41. Gross, J. E. et al. An evaluation of SERI surgical scaffold for soft-tissue support and repair in an ovine model of two-stage breast reconstruction. *Plast. Reconstr. Surg.* **134**, 700–704 (2014).
42. Wang, Y. et al. In vivo degradation of three-dimensional silk fibroin scaffolds. *Biomaterials* **29**, 3415–3428 (2008).
43. Wu, J. et al. Tuning the biodegradation rate of silk materials via embedded enzymes. *ACS Biomater. Sci. Eng.* **10**, 2607–2615 (2024).
44. Tanneberger, A. M. et al. Multinucleated giant cells within the in vivo implantation bed of a collagen-based biomaterial determine its degradation pattern. *Clin. Oral Investig.* **25**, 859–873 (2021).
45. Zhou, Q. ABAQUS User-defined field (USDFLD) subroutine for stochastic strength field. *Zenodo* <https://doi.org/10.5281/zenodo.18775588> (2026).
46. Lee, S. H. shlee8302/Silk_THzCode: Silk_THzCode. *Zenodo* <https://doi.org/10.5281/zenodo.18688272> (2026).
47. Wegst, U. G., Bai, H., Saiz, E., Tomsia, A. P. & Ritchie, R. O. Bioinspired structural materials. *Nat. Mater.* **14**, 23–36 (2015).

Acknowledgements

We thank A. Berenov and R. Whiteley for help with X-ray diffraction measurements and analysis; K. Li and Y. Lyu for nano-indentation data collection; Y. Wang, H. Yuan, Y. Hu and B. Peng for experimental and technical assistance; Y.-T. L. Dingle for her assistance with the schematic preparation; and H. Zou for fruitful discussions at the beginning of this work. Q.Z. (202106120057) is grateful to the China Scholarship Council for its financial support. We are grateful for the financial support from National Science Foundation (NSF) and specifically for grant no. 2243104, Center for Complex Particle Systems (COMPASS); grant no. 2317423 Lock-and-Key Interactions of Proteins and Chiral Nanoparticles, grant no. 2418861 CBET-EPSC Chiroptical Second-Harmonic Scattering of Nanostructures and Their

Biocomplexes. This work was also supported by the Tufts Launchpad | Accelerator grant (TLA, C.L.); the Air Force Office of Scientific Research (AFOSR, FA9550-23-1-0606, D.L.K.); the Engineering and Physical Sciences Research Council (EPSRC, EP/V037234/1 and EP/V037234/2, H.Z.); the Engineering and Physical Sciences Research Council New Investigator Award (EPSRC, EP/V049259/1, W.T.); the UK Research and Innovation Horizon Europe funding guarantee (UKRI, EP/Y037103/1, W.T.); the Engineering and Physical Sciences Research Council (EPSRC, EP/W022508/1, S.P.); the Austrian Science Fund (FWF, 10.55776/P33613, C.R. and S.S.); the Key Science and Technology Project of Henan Province (232102521001, X.W.); and the Major Science and Technology Project of Henan Province (241100310100, X.W.).

Author contributions

Q.Z. and E.B. conceived the idea and guided the overall project. X.W., S.P., C.R., W.T., H.Z., D.G.P., D.L.K., N.A.K., C.L. and E.B. supervised the research. Q.Z., X.Y., C.Z., S.S. and W.W. performed the experiments and characterizations. S.H.L., B.P., J.K. and N.A.K. designed and conducted the THz optical experiments and analysed the obtained results. Y.W., B.L., G.L. and C.L. conducted in vivo studies, histological analysis and discussed the results. Q.Z. and J.N. carried out 2D WAXS measurement and analysis. Q.Z., S.H.L., C.L. and E.B. wrote the original draft. All the authors reviewed and edited the paper and Supplementary Information.

Competing interests

The authors declare no competing interests.

Additional information

Extended data is available for this paper at <https://doi.org/10.1038/s41893-026-01821-y>.

Supplementary information The online version contains supplementary material available at <https://doi.org/10.1038/s41893-026-01821-y>.

Correspondence and requests for materials should be addressed to Nicholas A. Kotov, Chunmei Li or Emiliano Bilotti.

Peer review information *Nature Sustainability* thanks Zunfeng Liu, Luca Valentini and the other, anonymous, reviewer(s) for their contribution to the peer review of this work. Peer reviewer reports are available.

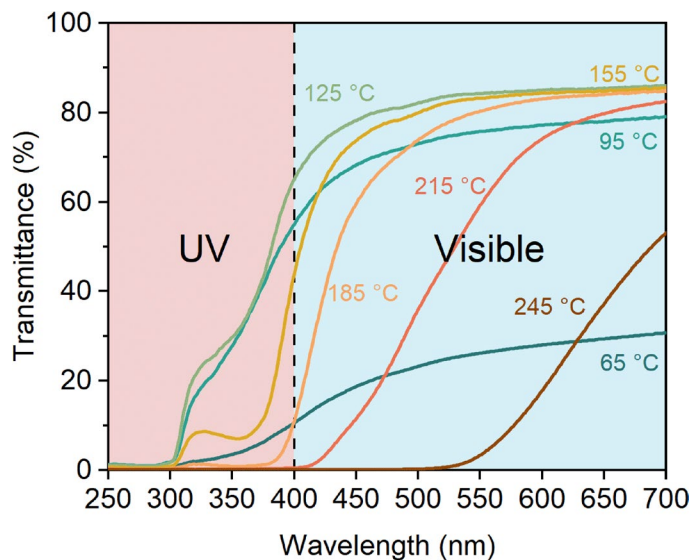
Reprints and permissions information is available at www.nature.com/reprints.

Publisher's note Springer Nature remains neutral with regard to jurisdictional claims in published maps and institutional affiliations.

Open Access This article is licensed under a Creative Commons Attribution 4.0 International License, which permits use, sharing, adaptation, distribution and reproduction in any medium or format, as long as you give appropriate credit to the original author(s) and the source, provide a link to the Creative Commons licence, and indicate if changes were made. The images or other third party material in this article are included in the article's Creative Commons licence, unless indicated otherwise in a credit line to the material. If material is not included in the article's Creative Commons licence and your intended use is not permitted by statutory regulation or exceeds the permitted use, you will need to obtain permission directly from the copyright holder. To view a copy of this licence, visit <http://creativecommons.org/licenses/by/4.0/>.

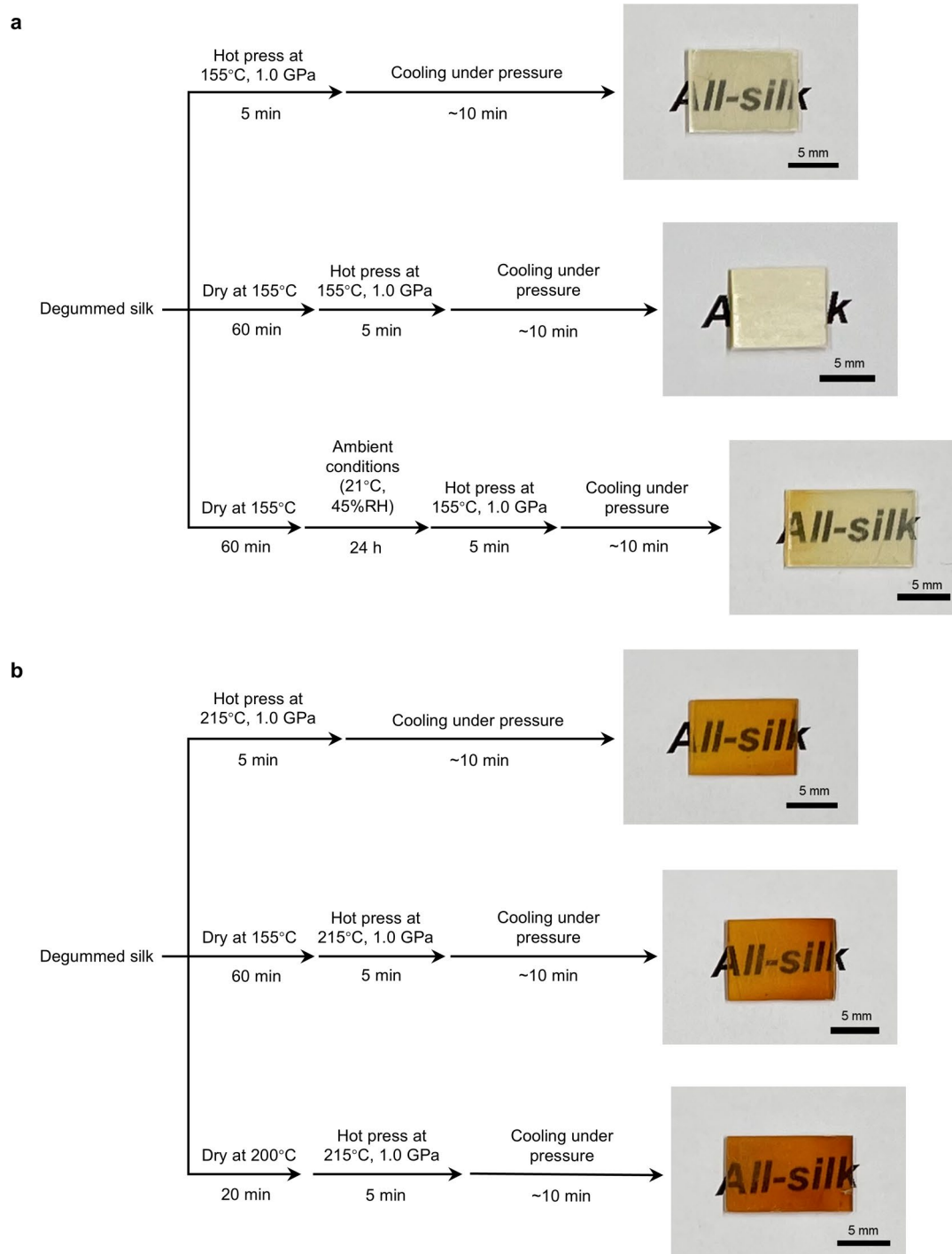
© The Author(s) 2026

¹Department of Aeronautics, Imperial College London, London, UK. ²School of Engineering and Materials Science, Queen Mary University of London, London, UK. ³School of Materials Science and Engineering, Xiangtan University, Xiangtan, China. ⁴Department of Plastic, Reconstructive and Aesthetic Surgery, Medical University of Vienna, Vienna, Austria. ⁵Department of Electrical Engineering and Computer Science, University of Michigan, Ann Arbor, MI, USA. ⁶Biointerfaces Institute, University of Michigan, Ann Arbor, MI, USA. ⁷University of Michigan, Department of Chemical Engineering, NSF Center for Science and Technology for Complex Particle Systems (COMPASS), Ann Arbor, MI, USA. ⁸Department of Biomedical Engineering, Tufts University, Medford, MA, USA. ⁹Department of Chemical Engineering, University of Michigan, Ann Arbor, MI, USA. ¹⁰Department of Materials Science and Engineering, Korea University, Seoul, Republic of Korea. ¹¹Imaging and Analysis Centre, Natural History Museum, London, UK. ¹²School of Mechanics and Safety Engineering, Zhengzhou University, Zhengzhou, China. ¹³National Center for International Research of Micro-Nano Molding Technology, Zhengzhou University, Zhengzhou, China. ¹⁴WMG, University of Warwick, Coventry, UK. ✉e-mail: kotov@umich.edu; chunmei.li@tufts.edu; e.bilotti@imperial.ac.uk



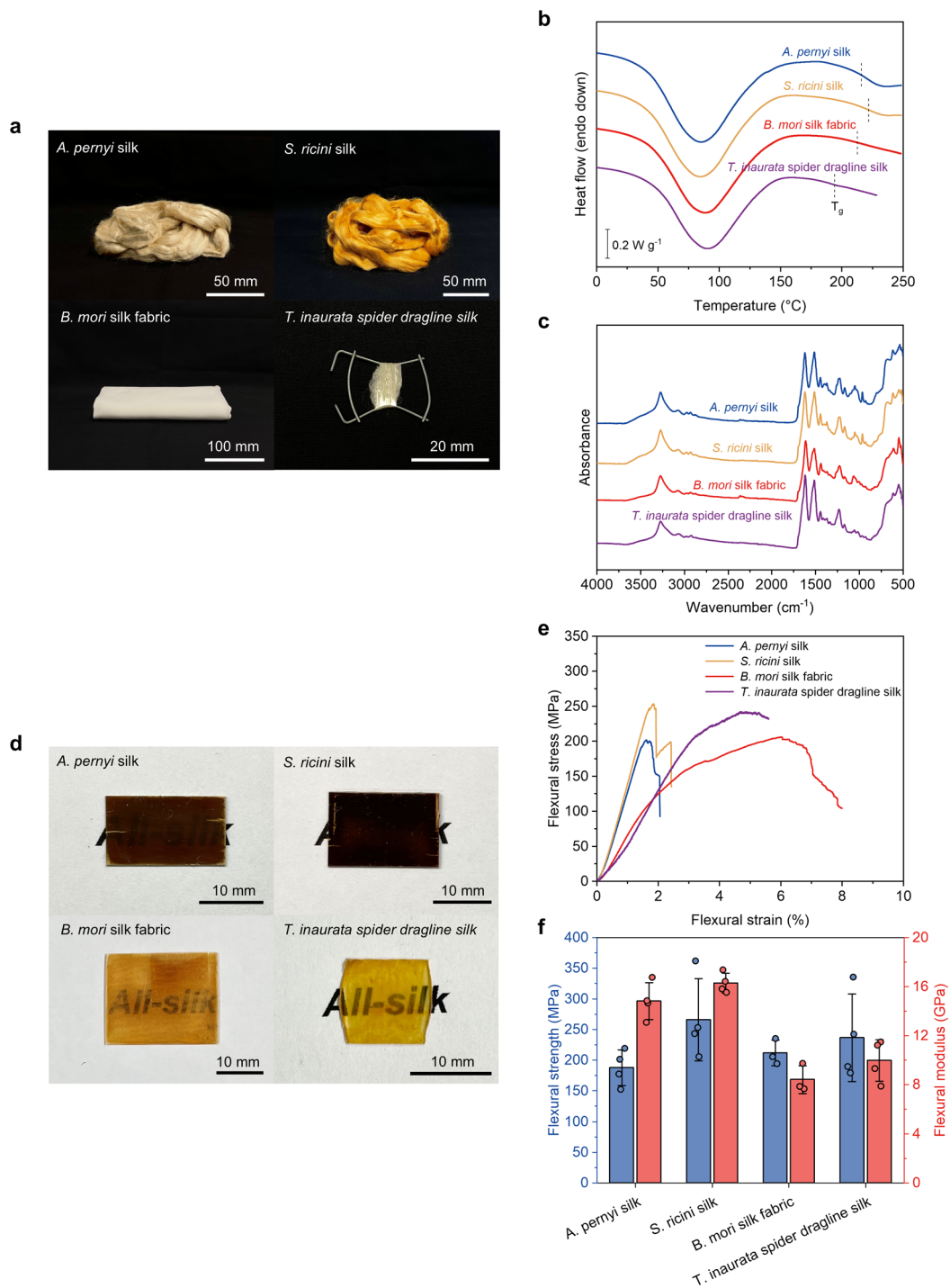
Extended Data Fig. 1 | UV-vis spectra of fused silk materials fabricated at different temperatures (1.0 GPa). The non-fused sample (65 °C) exhibits the lowest transmittance (~30%) across the visible range. In contrast, samples processed at 125, 155, 185 and 215 °C show consistently high transmittance, beginning at ~83% at 700 nm. The degraded specimen (245 °C) displays two

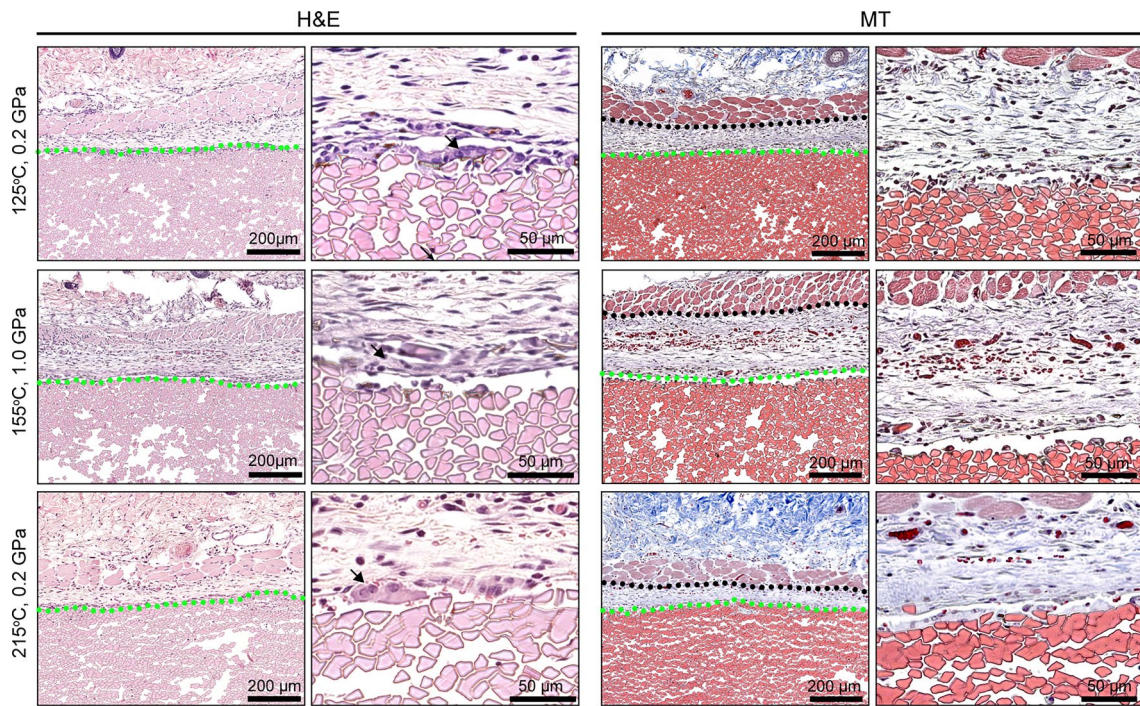
characteristic optical signatures: moderate transmittance (~50%) at 700 nm, and near-complete absorption (<1% transmittance) below 500 nm, indicative of protein degradation. These quantitative spectra, together with sample photographs, enable clear differentiation between non-fused, fused and degraded states.



Extended Data Fig. 2 | Experimental design for studying the role of water molecules in the formation of fused silk. a, At a low processing temperature (155 °C), water molecules act as an essential plasticiser: degummed silk fibres or fibres rehydrated after pre-drying can fuse to form transparent materials, whereas thoroughly dried fibres fail to fuse. **b,** At a higher processing

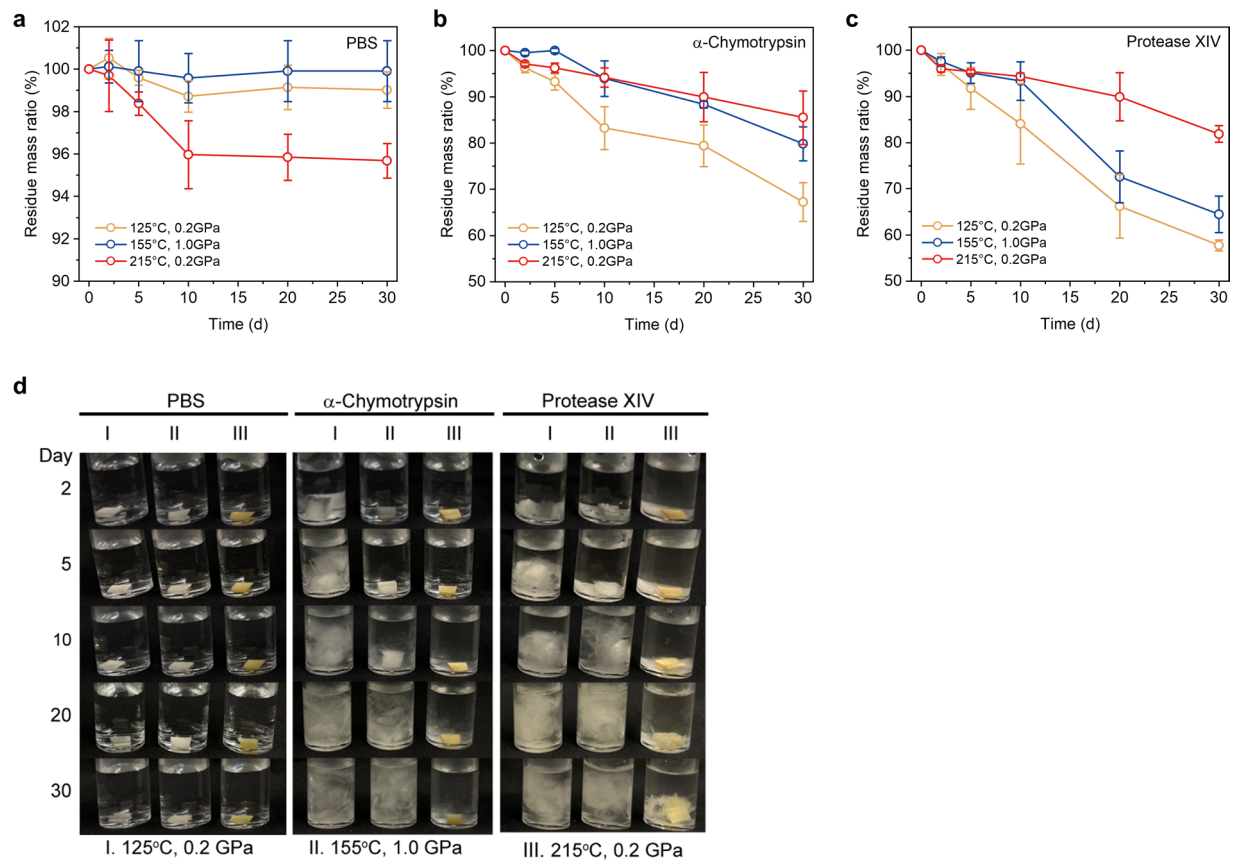
temperature (215 °C), close to the glass-transition region of silk, fibre fusion occurs even when water molecules have mainly been removed. These results indicate that water plasticisation enables molecular mobility at lower temperatures, whereas at higher temperatures the thermally activated diffusion of the amorphous phase alone is sufficient to drive silk fusion.





Extended Data Fig. 4 | The representative histological images of H&E and Masson's Trichrome staining of the samples after 7 days of subcutaneous implantation. The fibrous capsule is determined from the blue collagen layer

in Masson's trichrome staining and depicted by the region between the black and green dotted lines. Green-dashed lines in images indicate the implant-tissue interface, and black arrows indicate foreign body giant cells.



Extended Data Fig. 5 | In vitro degradation test. **a-c**, In vitro degradation profiles of fused silk in PBS solution (**a**), α -Chymotrypsin (40 U mL^{-1}) PBS solution (**b**) and protease XIV (5 U mL^{-1}) PBS solution (**c**). Data are presented as mean \pm s.d.

($n = 3$ independent samples). **d**, Photographs of fused silk incubated in PBS solution, α -Chymotrypsin (40 U mL^{-1}) PBS solution and protease XIV (5 U mL^{-1}) PBS solution for different times.

Reporting Summary

Nature Portfolio wishes to improve the reproducibility of the work that we publish. This form provides structure for consistency and transparency in reporting. For further information on Nature Portfolio policies, see our [Editorial Policies](#) and the [Editorial Policy Checklist](#).

Statistics

For all statistical analyses, confirm that the following items are present in the figure legend, table legend, main text, or Methods section.

n/a Confirmed

- The exact sample size (n) for each experimental group/condition, given as a discrete number and unit of measurement
- A statement on whether measurements were taken from distinct samples or whether the same sample was measured repeatedly
- The statistical test(s) used AND whether they are one- or two-sided
Only common tests should be described solely by name; describe more complex techniques in the Methods section.
- A description of all covariates tested
- A description of any assumptions or corrections, such as tests of normality and adjustment for multiple comparisons
- A full description of the statistical parameters including central tendency (e.g. means) or other basic estimates (e.g. regression coefficient) AND variation (e.g. standard deviation) or associated estimates of uncertainty (e.g. confidence intervals)
- For null hypothesis testing, the test statistic (e.g. F , t , r) with confidence intervals, effect sizes, degrees of freedom and P value noted
Give P values as exact values whenever suitable.
- For Bayesian analysis, information on the choice of priors and Markov chain Monte Carlo settings
- For hierarchical and complex designs, identification of the appropriate level for tests and full reporting of outcomes
- Estimates of effect sizes (e.g. Cohen's d , Pearson's r), indicating how they were calculated

Our web collection on [statistics for biologists](#) contains articles on many of the points above.

Software and code

Policy information about [availability of computer code](#)

Data collection

TGA, DSC and DMTA data were collected by TA Instruments TRIOS 5.1.1. 2D SAXS data were collected by Malvern Panalytical Data Collector software. FTIR data were collected by Bruker OPUS 8.5.29. UV-vis data were collected by PerkinElmer UV WinLab software. 2D WAXS data were collected by the RINT RAPID control software. Mechanical test data were collected by Instron Bluehill and Bluehill LE software. Finite element simulations were conducted using ABAQUS 2022. THz data were collected by MATLAB 2025a. The ABAQUS user-defined field (USDFLD) subroutine used to implement the stochastic strength field in the finite element analysis of fused silk is available via Zenodo (<https://doi.org/10.5281/zenodo.18775588>). The custom code used for the silk THz experiments is available via Zenodo (<https://doi.org/10.5281/zenodo.18688272>).

Data analysis

TA Instruments TRIOS 5.1.1 was used to analyse the data of TGA, DSC and DMTA. PeakFit v4.12 was used to analyse the data of FTIR and XRD. XRD2DScan 6.0 was used to analyse the 2D SAXS data. Rigaku 2DP software was used to analyse the 2D WAXS data. Photron PFV4 was used to analyse the data of the ballistic test. ImageJ 1.54g was used to analyse the SEM and histology images. MATLAB 2025a with custom code was used for analysis and calculation of the THz data. GraphPad Prism 9 was used for all statistical analysis. Origin 2018 was used to analyse and visualise all the data.

For manuscripts utilizing custom algorithms or software that are central to the research but not yet described in published literature, software must be made available to editors and reviewers. We strongly encourage code deposition in a community repository (e.g. GitHub). See the Nature Portfolio [guidelines for submitting code & software](#) for further information.

Data

Policy information about [availability of data](#)

All manuscripts must include a [data availability statement](#). This statement should provide the following information, where applicable:

- Accession codes, unique identifiers, or web links for publicly available datasets
- A description of any restrictions on data availability
- For clinical datasets or third party data, please ensure that the statement adheres to our [policy](#)

All data that support the findings of this study are available in the paper and Supplementary Information. Source data are provided with this paper.

Research involving human participants, their data, or biological material

Policy information about studies with [human participants or human data](#). See also policy information about [sex, gender \(identity/presentation\), and sexual orientation](#) and [race, ethnicity and racism](#).

Reporting on sex and gender	N/A
Reporting on race, ethnicity, or other socially relevant groupings	N/A
Population characteristics	N/A
Recruitment	N/A
Ethics oversight	N/A

Note that full information on the approval of the study protocol must also be provided in the manuscript.

Field-specific reporting

Please select the one below that is the best fit for your research. If you are not sure, read the appropriate sections before making your selection.

- Life sciences
 Behavioural & social sciences
 Ecological, evolutionary & environmental sciences

For a reference copy of the document with all sections, see [nature.com/documents/nr-reporting-summary-flat.pdf](https://www.nature.com/documents/nr-reporting-summary-flat.pdf)

Ecological, evolutionary & environmental sciences study design

All studies must disclose on these points even when the disclosure is negative.

Study description	We developed a rapid thermo-mechanical method to fuse silk fibres into solid materials while preserving their hierarchical structure. The fused silk material shows record-high mechanical properties, tuneable biocompatibility and biodegradability, optical transparency, and strong terahertz optical response. The direct conversion of silk fibres into high-performance structural and optically-active materials enhances the prospects for their scalable production and real-world deployment.
Research sample	Bombyx mori silk and fused silk materials fabricated by thermo-mechanical method.
Sampling strategy	N/A
Data collection	All data were collected by standard methods. Details are provided in the Methods section of the main text and Supplementary Information.
Timing and spatial scale	Data were collected from October 2021 to June 2025.
Data exclusions	N/A
Reproducibility	All attempts to repeat the experiment were successful.
Randomization	All samples in this work were tested randomly.
Blinding	N/A

Did the study involve field work? Yes No

Reporting for specific materials, systems and methods

We require information from authors about some types of materials, experimental systems and methods used in many studies. Here, indicate whether each material, system or method listed is relevant to your study. If you are not sure if a list item applies to your research, read the appropriate section before selecting a response.

Materials & experimental systems

- n/a Involved in the study
- Antibodies
- Eukaryotic cell lines
- Palaeontology and archaeology
- Animals and other organisms
- Clinical data
- Dual use research of concern
- Plants

Methods

- n/a Involved in the study
- ChIP-seq
- Flow cytometry
- MRI-based neuroimaging

Animals and other research organisms

Policy information about [studies involving animals](#); [ARRIVE guidelines](#) recommended for reporting animal research, and [Sex and Gender in Research](#)

Laboratory animals	Eight-week-old C57BL/6 mice
Wild animals	No wild animals were used.
Reporting on sex	According to current scientific understanding, subcutaneous foreign body encapsulation is largely sex-independent, with no significant differences reported in routine biocompatibility assessments. Therefore, only male mice were used in this work for consistency.
Field-collected samples	No field-collected samples were used.
Ethics oversight	The animal study was reviewed and approved by the Institutional Animal Care and Use Committee of Tufts University (animal protocol M2022-121). Mice (5 mice per cage) were housed in a specific pathogen-free environment at a temperature of 18–22°C and a humidity of 50–60%, with a dark/light cycle of 12h. All mice were promptly euthanized using CO ₂ gas after finishing animal experiment.

Note that full information on the approval of the study protocol must also be provided in the manuscript.

Plants

Seed stocks	<i>Report on the source of all seed stocks or other plant material used. If applicable, state the seed stock centre and catalogue number. If plant specimens were collected from the field, describe the collection location, date and sampling procedures.</i>
Novel plant genotypes	<i>Describe the methods by which all novel plant genotypes were produced. This includes those generated by transgenic approaches, gene editing, chemical/radiation-based mutagenesis and hybridization. For transgenic lines, describe the transformation method, the number of independent lines analyzed and the generation upon which experiments were performed. For gene-edited lines, describe the editor used, the endogenous sequence targeted for editing, the targeting guide RNA sequence (if applicable) and how the editor was applied.</i>
Authentication	<i>Describe any authentication procedures for each seed stock used or novel genotype generated. Describe any experiments used to assess the effect of a mutation and, where applicable, how potential secondary effects (e.g. second site T-DNA insertions, mosaicism, off-target gene editing) were examined.</i>